ADVANCED FUNCTIONAL MATERIALS
www.afm-journal.de

Chloride-Mediated Electron Buffering on Ni-Fe Anodes for Ampere-Level Alkaline Seawater Electrolysis

Qian Niu, Fei-Yue Gao, Xiaogang Sun, Yao Zheng, and Shi-Zhang Qiao**

In water electrolysis, the long-term stability of anodes is compromised by their degradation under oxidative conditions. This issue becomes more pronounced in seawater electrolysis, where the natural chloride ion (Cl^-) induces the chlorine evolution reaction (ClER) to produce corrosive byproducts. Herein, a series of small organic molecules (SOMs), featuring an aromatic carbon ring with para-positioned carbonyl groups, are integrated with the conventional nickel-iron (Ni-Fe) based anode. This integration triggers a unique electron buffering effect to address anode degradation in natural seawater-based electrolytes. It is found that preferential adsorption of Cl^- onto SOMs prevents its direct interaction with metal active sites. Furthermore, SOM-Cl serving as an electron buffering group significantly reduces the dissolution of Fe sites under the highly oxidative environment. As a result, the SOM-Cl-engineered anode enhances oxygen evolution activity by ≈1.7 times in seawater compared to pure water. In addition, the rationally designed anode works stably for over 200 h at a high current density of 1.3 A cm^{-2} in an alkaline seawater electrolyzer (ASE).

1. Introduction

In coastal areas with abundant renewable energy, direct seawater electrocatalysis offers a cost-effective method to produce hydrogen.[1] Considering the complex composition of seawater, alkaline electrolyzers (AEs) using non-precious electrodes and durable polymer diaphragms enable operation with relatively seawater.[2] However, due to the high concentration chloride ions (Cl^-) in seawater, addressing anode degradation in seawater is more challenging than in freshwater.[3] The uncontrolled chlorine evolution reaction (ClER) generates corrosive hypochlorite ions (OCl^-), which induce anode corrosion through oxidative etching.[4] Such damage to the anode always results in the loss of active sites of electrocatalysts,[5] leading to a more intense oxidative environment, which accelerates anode degradation exponentially.

In recent years, hydrogen production at ampere-level current densities has been widely advocated to achieve higher efficiency.[6] Although the technology has been successfully operated in pure water systems at ampere-level current densities, its application in natural seawater environments remains challenging. Specifically, achieving ampere-level hydrogen production in seawater results in more severe anode degradation due to intensified Cl^--induced corrosion combined with the highly oxidative environment.[7] Some previous strategies focused on repelling Cl^- from the anode surface.[8] These strategies require anchoring Cl^--repelling sites on the anode,[9] which significantly reduces the valuable active area for oxygen evolution reaction (OER). Anchoring Cl^--repelling sites on the anode also needs to consider the potential decline in mechanical properties of the anode. In addition, these strategies merely focus on physical defense,[10] do not provide specific protection against Cl^-. Therefore, these strategies do not show their potential in ampere-level seawater electrolysis.[11]

Notably, several earlier works have cleverly utilized Cl^- to enhance the performance of anode for seawater electrolysis.[12] The direct adsorption of Cl^- on metal sites in electrocatalysts can switch the mechanism of the OER and repel the bulk Cl^- in seawater, which provides better stability for electrocatalysts compared to pure water. However, without a robust electron regulation moiety to control the electron transfer from Cl^- to anode, the direct bonding of Cl^- on a metal active site will increase the risk of ClER. Therefore, most alkaline seawater electrolyzers (ASEs) are operated at a current density of ≈0.5 A cm^{-2}; while achieving stable operation at ampere-level current densities remains a significant challenge.[13]

Herin, we constructed a functionalized small organic molecule (SOM) layer on the nickel-iron (Ni-Fe) anode surface to capture Cl^-. The attached dicarbonyl group enables SOM to interact simultaneously with metal sites in electrocatalysts and bulk Cl^- in the electrolyte, forming a SOM-Cl transition layer. With preventing direct bonding between Cl^- and metal sites by SOM, the chemical states of the anode surface are efficiently regulated, minimizing the production of corrosive OCl^-. Meanwhile, following the formation of SOM-Cl, the conjugated π

Q. Niu, F.-Y. Gao, X. Sun, Y. Zheng, S.-Z. Qiao
School of Chemical Engineering
The University of Adelaide
Adelaide 5005, Australia
E-mail: yao.zheng01@adelaide.edu.au; s.qiao@adelaide.edu.au

The ORCID identification number(s) for the author(s) of this article can be found under https://doi.org/10.1002/adfm.202504872

DOI: 10.1002/adfm.202504872

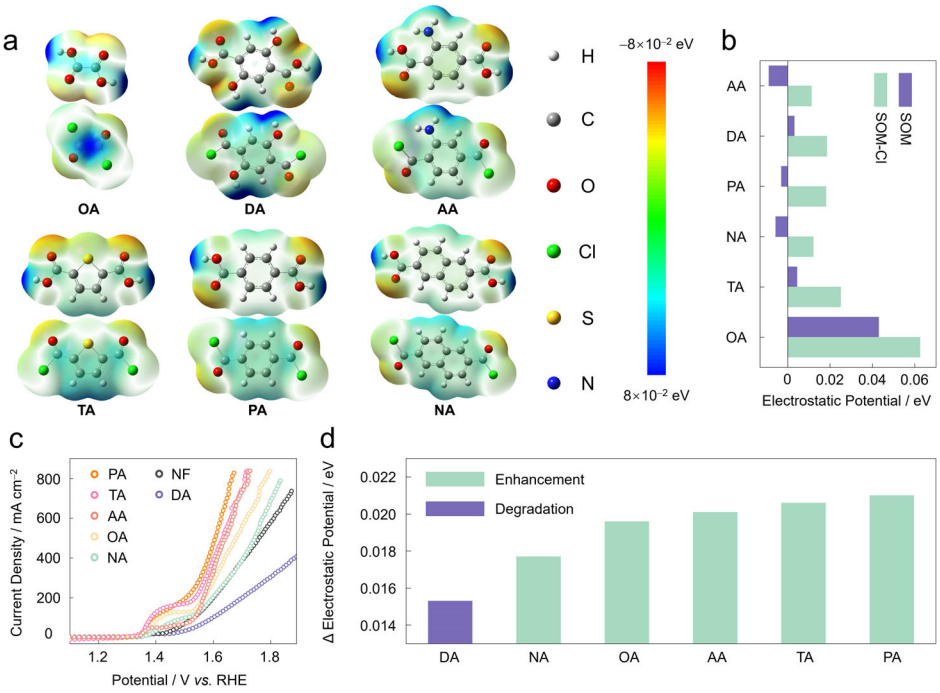

Figure 1. Preliminary investigation into SOM-Cl properties. a) Electrostatic potential maps of six SOMs in both non-adsorbed and Cl^--adsorbed states. The top images represent the non-adsorbed state, while the bottom images correspond to the Cl^--adsorbed state. b) Comparison of the electrostatic potential at the molecule center between SOM and SOM-Cl. c) The LSV curves of the SOM-modified electrocatalysts in simulated seawater (0.5 M NaCl + 1 M KOH). d) Increased electrostatic potential values at the molecule center of SOM following Cl^- adsorption.

electrons within SOM are modified, which lowers the OER overpotential by ≈400 mV at 1 A cm^{-2} and mitigates the oxidative damage to the anode. Compared to SOM, SOM-Cl species significantly mitigate oxidative damage and effectively suppress the dissolution of active sites at an ampere-level current density operation. As a result, an ASE achieves stable operation for over 200 h under the current densities of 1.3 A cm^{-2} in seawater splitting.

2. Results and Discussion

2.1. Preanalysis of SOM-Cl

Six SOMs containing both aromatic carbon ring and dicarbonyl were selected to construct functionalized layer, including oxalic acid (OA), 2,5-dihydroxyterephthalic acid (DA), 2-aminoterephthalic acid (AA), 2,5-thiophenedicarboxylic acid (TA), p-phthalic acid(PA), and 2,6-naphthalenedicarboxylic acid (NA). The functionalized layer is constructed through a hydrothermal method (see experimental section). Their dicarboxylic structure can simultaneously adsorb Cl^- and anchor itself to Ni-Fe based OER electrocatalyst (e.g., Ni-Fe oxide/hydroxide). After constructing the SOM layer on the electrocatalyst surface, the distinct linear sweep voltammetry (LSV) curves suggest that SOM modification is effective only when Fe is present in the electrocatalyst (Figure S1, Supporting Information). Therefore, compared to Ni, Fe sites are likely the interaction sites with SOM. After modification with these SOMs, Ni-Fe oxide/hydroxide (NF) generally retains their original crystal structure and morphology, as evidenced by the X-ray diffraction (XRD) patterns and the scan electron microscopy images (Figures S2 and S3, Supporting Information). The operando Raman spectra confirm that Cl^- is adsorbed by the carbonyl groups (Figure S4, Supporting Information). To compare the electrostatic potential distribution of different SOMs after Cl^- adsorption, we calculated the electrostatic potential maps of six SOMs with both non-adsorbed and Cl^--adsorbed states. Due to differences of their conjugated structures, SOMs show various electrostatic potential distributions after Cl^- adsorption (**Figure 1a**). After Cl^- adsorption, the electrostatic potential at the molecular center increases across all six SOMs (Figure 1b). Afterward, the OER performance of SOM-modified electrocatalysts was evaluated. Compared to unmodified NF electrocatalysts, the performance of six SOM-modified electrocatalysts varies significantly. Within the voltage range of 1.57–1.87 V on the LSV curves, the response current densities of the six SOM-modified electrocatalysts follow the order of PA, TA, AA, OA, NA, and DA (Figure 1c). Correspondingly, after Cl^- adsorption, the electrostatic potential differences between non-adsorbed and Cl^--adsorbed SOMs also follow the order of PA, TA, AA, OA, NA, DA, ranging from 0.0153 to 0.021 eV (Figure 1d). This suggests that there may be a positive relationship between electrostatic potential and OER performance. Among the six SOMs, PA shows the largest change in electrostatic potential after Cl^- adsorption, indicating its strongest ability to enhance the OER performance of NF.

2.2. Electron Buffering Effect

To thoroughly understand the relationship between the electrostatic potential and the enhanced OER performance, current density differences between SOM-modified electrocatalysts and

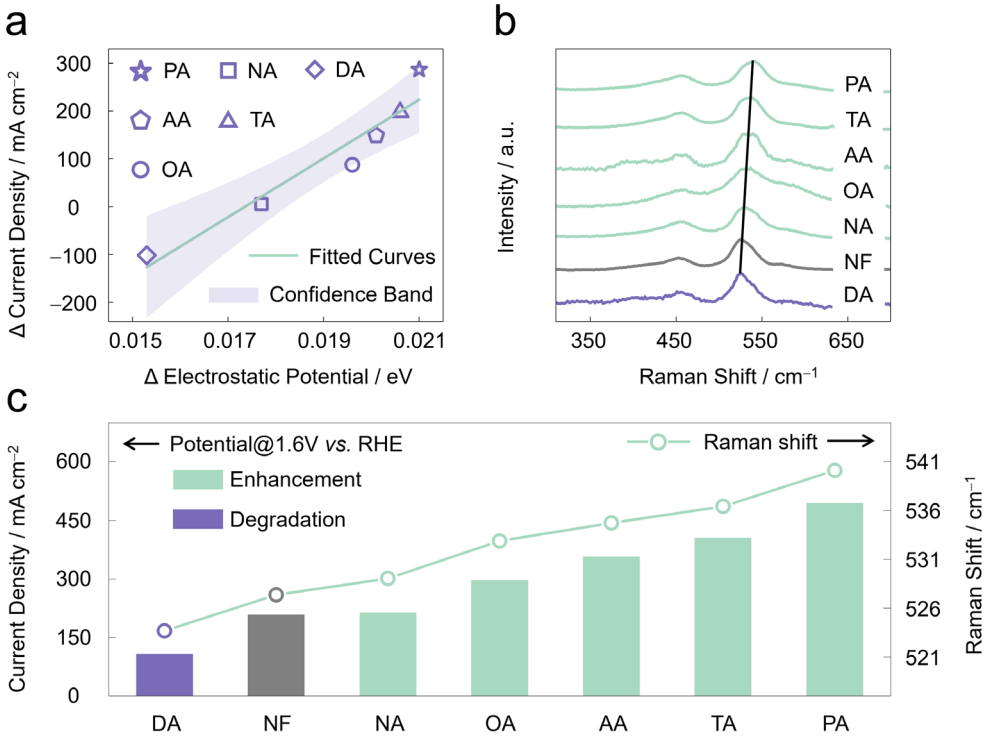

Figure 2. Causes of the electron buffering effect. a) The linear relationship between the electrostatic potential difference and the current density difference. b) Raman spectra in the selective range of 310–700 cm^{-1} for SOM-modified electrocatalysts after LSV test in simulated seawater (0.5 M NaCl + 1 M KOH). c) The relationship between current densities and Raman shifts of the SOM modified electrocatalysts.

unmodified NF electrocatalysts were incorporated into the subsequent analysis. As shown in **Figure** 2a, the electrostatic potential difference between SOM and SOM-Cl correlates linearly with the current density difference. This relationship indicates that the electrostatic potential difference is the direct factor to enhance the OER performance of the SOM-modified electrocatalysts. It is worth noting that all six selected data points for fitting fall within the confidence band, suggesting that the fitting results are reliable. Regarding the electrostatic potential difference that enhances OER performance, it is speculated that Cl^- could alter the original electrostatic potential state of SOM, consequently changing the chemical state of the adjacent metal sites. To verify this hypothesis, Raman spectroscopy is utilized to characterize the chemical state of the metal sites.

As shown in Figure 2b, the PA-modified electrocatalyst exhibits the largest blue shift at the peak corresponding to the Ni-O bond stretching vibration (marked by the black line),[14] while the DA-modified electrocatalyst exhibits the smallest feature. Further analysis reveals a positive correlation between the current densities and the Raman peak positions, the greater blue shift corresponds to the better OER performance (Figure 2c). Combining the positive relationship between electrostatic potential and OER performance discussed above, we infer that the electrostatic potential difference induced by Cl^- adsorption affects the chemical state of the nearby metal sites, thereby influencing the OER process occurring at these sites. This suggests that in the Cl^--containing environment, the interaction between SOM and Cl^- forms a SOM-Cl electron buffering group, which leverages its abundant conjugated π electrons to optimize the OER process (Figure S5, Supporting Information).

2.3. Electron Buffering Group Regulates the Anode Surface Chemical State

Within SOM-Cl, the distinct conjugated structure of SOM effectively stabilizes the adsorbed Cl^-, thereby preventing its oxidation. Unlike uncontrolled direct bonding between Cl^- and metal (**Figure** 3a), ClER is effectively suppressed in SOM-Cl, enabling ampere-level selective OER. After SOM modification, the X-ray photoelectron spectra of the SOM-modified electrocatalyst reveal a new peak in the Fe 2p region, which suggests that Fe may serve as the interaction site with the SOM-Cl transition layer (Figure S6, Supporting Information). And the persistence of this new peak after the chronopotentiometry test indicates that SOM-Cl transition layer can stably anchor to the electrocatalyst during OER process (Figure S7, Supporting Information). Moreover, SOM-Cl transition layer generates a specific repulsion toward Cl^-, which hinders uncontrolled interaction between Cl^- and metal sites (Figure 3b). After the chronopotentiometry test, the surface Cl content of both SOM-modified electrocatalysts and unmodified electrocatalysts are analyzed using energy-dispersive X-ray spectroscopy. The results show that the surface of the SOM-modified electrocatalyst contains a lower amount of Cl species than unmodified electrocatalysts (Figure 3c). This suggests that the SOM-Cl layer can prevent excessive Cl^- buildup on the electrocatalyst surface. According to the cyclic voltammetry (CV) curves, the SOM-modified electrocatalysts exhibit a higher

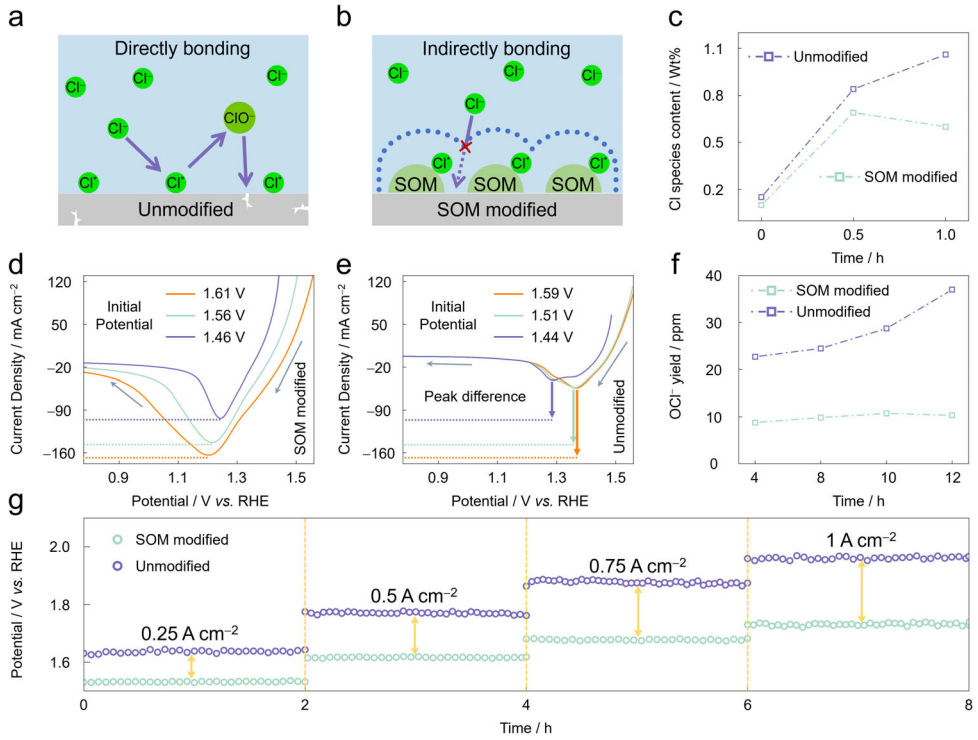

Figure 3. The regulated surface chemical state of the SOM-modified electrocatalyst. a) The schematic diagram illustrates the corrosion formation mechanism caused by the direct bonding between unmodified electrocatalysts and Cl^-. b) The schematic diagram illustrates that the ClER is suppressed due to the regulated surface chemical states. c) After chronopotentiometry test at 1 A cm^{-2}, variation of surface Cl species content over time for SOM modified electrocatalyst and unmodified electrocatalyst. d) The CV curves with different initial potentials of SOM modified electrocatalysts. e) The CV curves with different initial potentials of unmodified electrocatalysts. f) The yield of OCl^- at 1 A cm^{-2} overtime for SOM-modified electrocatalysts and unmodified electrocatalysts. g) Multistep chronopotentiometry plots for SOM-modified electrocatalysts and unmodified electrocatalysts under different current densities.

reduction peak than unmodified electrocatalysts across various initial voltages (Figure 3d,e). For the SOM-modified electrocatalysts, Cl^- is merely adsorbed by SOM without being oxidized, which leads to changes in the capacitive properties, whereas the unmodified electrocatalysts behave differently. Thus, the ClER was effectively suppressed in the SOM-modified electrocatalysts, as the ion chromatography results shown in Figure 3f. Additionally, across various current densities, the SOM-modified electrocatalyst also maintains a lower OCl^- yield than the unmodified electrocatalyst (Figure S8, Supporting Information). Due to the low yield rate of corrosive OCl^-, SOM modified electrocatalyst can maintain its microstructure during seawater electrolysis, while the unmodified electrocatalyst cannot, as evidenced by transmission electron microscope images (Figure S9, Supporting Information). The multistep chronopotentiometry plots show that the voltage gap between SOM-modified electrocatalysts and unmodified electrocatalysts widens, which may be attributed to the gradual formation of SOM-Cl layer (Figure 3g).

2.4. Electron Buffering Group Improves the Anode Performance

During sweater electrolysis, the abundant Cl^- adsorbs onto SOM, forming SOM-Cl. In this process, the electron structure of SOM is modified, which affects the chemical states of nearby metal sites and results in enhanced OER activity. The LSV curves measured in different electrolytes with varying Cl^- concentrations show that as the Cl^- concentration increases, the OER performance gradually improves (**Figure 4a**). Notably, to eliminate the influence of conductivity, we replaced sodium chloride (NaCl) with sodium sulfate (Na_2SO_4). During CV tests, electrolytes with higher Cl^- concentrations corresponded to higher reduction current densities (Figure 4b), which may be due to the affected meatal sites. After the chronopotentiometry test, the improved LSV curves also reveal that Cl^- enhances OER performance via preferential adsorption onto SOM (Figure S10, Supporting Information). Aside from improving activity, the SOM-Cl also enhances stability by counteracting the highly oxidative environment. As illustrated in Figure 4c, the preferential adsorption of Cl^- modifies the conjugated structure of SOM, thereby suppressing oxidative degradation induced by the highly oxidative environment. In operando Raman spectra (Figure 4d), two characteristic peaks corresponding to E_g bending and A_{1g} stretching vibration of Ni-O were simultaneously observed in Cl^--containing and Cl^--free electrolyte for SOM modified electrocatalysts,[14] labeled as I_1 and I_2. After applying voltage, the anode continuously oxidizes water to produce oxygen. However, in this process, the degradation of Ni species can be easily triggered by a highly oxidative environment. As observed in the Cl^--free electrolyte, both the intensity and position of I_1 and I_2 exhibit notable changes as the voltage increases. This may indicate that the Ni species in the electrocatalyst undergoes an oxidation state transformation at high voltage. But in Cl^--containing electrolyte,

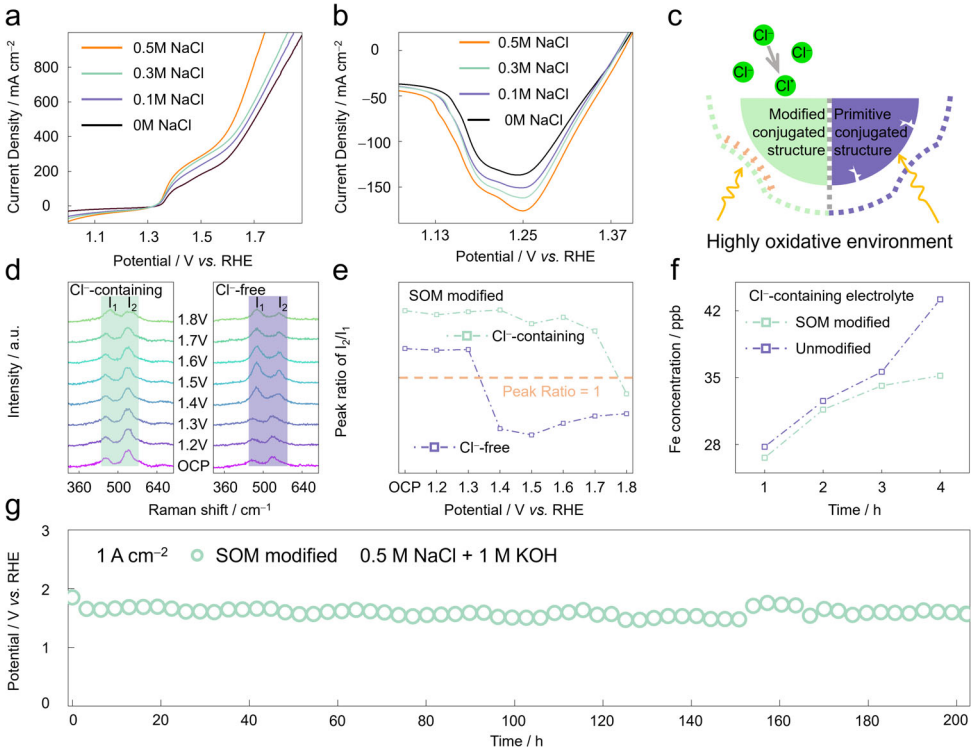

Figure 4. The electron buffering effect enhances OER performance. a) The LSV curves of SOM-modified electrocatalysts in gradient Cl^- electrolytes. b) The CV curves of the SOM-modified electrocatalysts in gradient Cl^- electrolytes. c) The schematic diagram illustrates that Cl^- modifies the conjugated structure to mitigate the damage caused by the highly oxidative environment, whereas the primitive conjugated structure cannot. d) Operando Raman spectra of SOM modified electrocatalysts in Cl^--containing electrolyte and Cl^--free electrolyte. e) Peak ratio of I_2/I_1 versus potential in Cl^--containing electrolyte and Cl^--free electrolyte. f) During chronopotentiometry tests at 1 A cm^{-2}, the variation of Fe content in electrolyte over time for SOM modified electrocatalysts and unmodified electrocatalysts. g) Chronopotentiometry plot of the SOM modified electrocatalysts at 1 A cm^{-2}.

the Ni species do not undergo significant transformation, as both the intensity and position of I_1 and I_2 do not change significantly with increasing voltage. In addition, the intensity ratio between I_2 and I_1 clearly reveals that the SOM-modified electrocatalysts can remain stable in Cl^--containing electrolyte even at the applied voltage of 1.8 V (Figure 4e). The above operando Raman results indicate that the SOM-Cl transition layer can buffer the oxidative damage caused by voltage. Therefore, compared to the unmodified electrocatalysts, the Fe leaching rate of the SOM-modified electrocatalysts is significantly reduced (Figure 4f). Additionally, the ammonium ions (NH_4^+) embedded in the lattice of NF, introduced during synthesis, also exhibit buffered degradation. The operando Fourier-transform infrared spectroscopy show the slow release of NH_4^+ in SOM-modified electrocatalysts, indicating that the SOM-Cl transition layer can mitigate the damage caused by voltage (Figures S11 and S12, Supporting Information). In contrast, without the SOM-Cl transition layer, the degradation of Ni species in unmodified electrocatalysts is more severe (Figure S13, Supporting Information). In a three-electrode system, the SOM-modified electrocatalysts maintain stability for over 200 h at a current density of 1 A cm^{-2} (Figure 4g). Apart from the three-electrode system, the SOM-modified electrocatalyst also demonstrates excellent stability in the two-electrode system. Using NiMo alloy as the cathode, the SOM-modified electrocatalyst can be operated for over 200 h at 1 A cm^{-2} in alkaline seawater (Figure S14, Supporting Information).

2.5. Performance of the Assembled ASE

During water electrolysis, the anode surface undergoes frequent three-phase turbulence.[15] The turbulence often induces intermittent voltage increases, causing anode degradation, which may be further exacerbated by insufficient electrolyte during AE operation. In industrial hydrogen production, AE is the most critical component. Therefore, to evaluate the potential of the SOM-modified electrocatalyst for industrial-scale seawater electrolysis, we assembled an ASE using NiMo alloy as a cathode and SOM-modified electrocatalyst as anode for seawater splitting (**Figure 5a**). The assembled ASE was tested at three different temperatures: 25, 45, and 65 °C. As anticipated, the ASE performance significantly improves at elevated temperatures due to the enhanced mass transfer, as evidenced by the LSV curves in Figure 5b. To thoroughly verify the stability performance of the SOM-modified electrocatalysts, the assembled ASE was tested under a high current density of 1.3 A cm^{-2}. As shown in Figure 5c,d, the assembled ASE can be operated stably for over 200 h at 1.3 A cm^{-2}, with negligible degradation. This performance is comparable or even superior to that of some reported ASEs (Table S1, Supporting Information). Following the ASE test, the XRD pattern of the SOM modified electrocatalyst shows no significant changes in its main diffraction peaks, confirming its structural stability (Figure S15, Supporting Information). Additionally, we also tested the assembled ASE at a lower

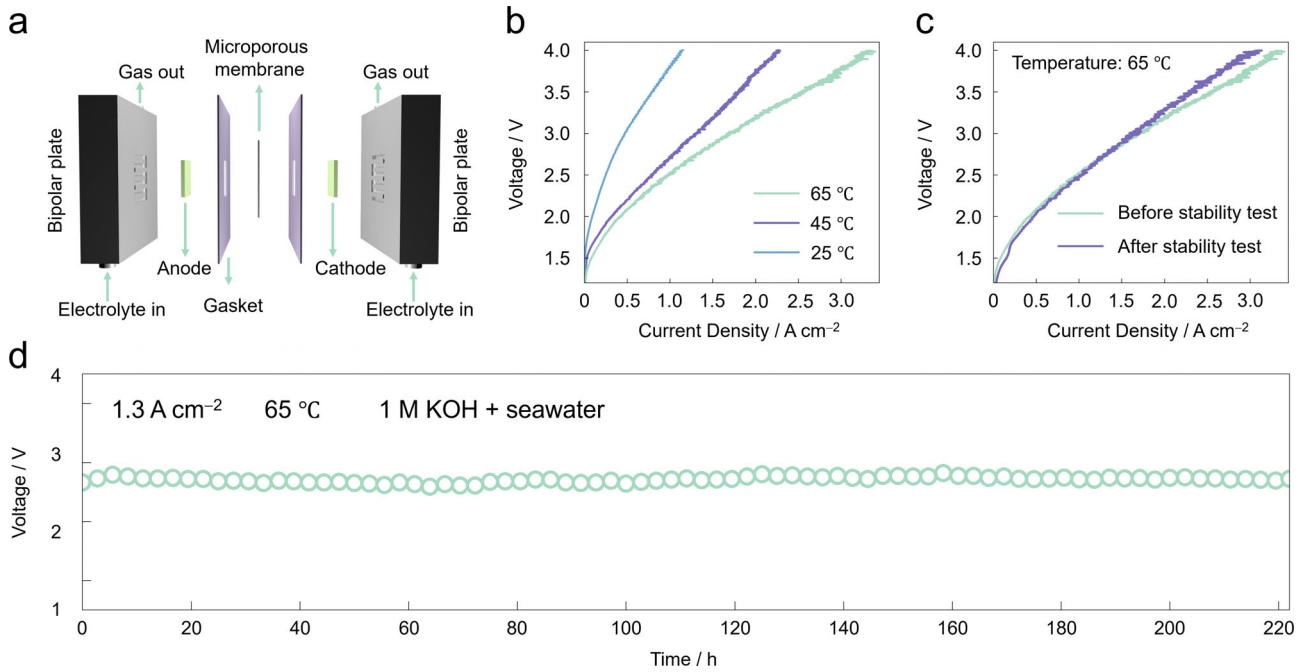

Figure 5. The performance of the assembled ASE. a) Schematic diagram of the assembled ASE. b) The LSV curves of assembled ASE using SOM-modified electrocatalysts || NiMo alloy in alkaline seawater (1.0 M KOH + seawater) at different temperatures. c) Comparison of LSV curves before and after stability test for ASE using SOM modified electrocatalysts || NiMo alloy in alkaline seawater (1.0 M KOH + seawater) at 65 °C. d) Stability test of the assembled ASE using SOM modified electrocatalysts || NiMo alloy at 1.3 A cm^{-2} in alkaline seawater (1.0 M KOH + seawater) at 65 °C.

temperature of 45 °C to artificially create a more oxidative environment. Under 45 °C, the assembled ASE can be operated stably for more than 110 h (Figure S16, Supporting Information), with LSV curves indicating minimal degradation (Figure S17, Supporting Information). The stable ASE operation indicates that the electron buffering group can effectively protect the anode under ampere-level current density. Notably, introducing the electron buffering effect into anode is a universal strategy for seawater electrolysis. To demonstrate its broad applicability, we synthesized additional Fe-containing electrocatalysts: manganese-iron oxide/hydroxide (MF), Ni—Fe alloy (NFA), and cobalt-iron oxide/hydroxide (CF). Their XRD patterns are shown in Figure S18 (Supporting Information). Similar to NF, these SOM-modified Fe-containing electrocatalysts all exhibit improved activity in Cl^--containing electrolyte (Figures S19 and S20, Supporting Information).

3. Conclusion

In summary, we proposed a SOM modification strategy to fabricate stable anodes in seawater electrolysis. The conjugated electrons of SOM are utilized to regulate the chemical state of the adsorbed Cl^-, which suppresses the formation of corrosive OCl^-. Meanwhile, the newly formed SOM-Cl transition layer on the anode selectively blocks bulk Cl^- in seawater, preventing excessive Cl^- accumulation on the anode surface. Furthermore, the SOM-Cl transition layer exhibits an electron buffering effect, regulating the chemical states of the adjacent metal sites, thereby reducing the overpotential of OER and mitigating the damage caused by the highly oxidative environment at the anode. As a result, the SOM-modified electrocatalysts achieve stable seawater electrolysis in an ASE for over 200 h at 1.3 A cm^{-2}. Unlike the previous study that focused solely on defending against the Cl^--induced corrosion in seawater, this work demonstrates that Cl^- can be effectively harnessed through preferential adsorption by SOM to enhance OER performance. Furthermore, the construction of a Cl-mediated electron buffering group offers a viable pathway for efficient green hydrogen production via seawater electrolysis.

4. Experimental Section

Synthesis of NF: NF was synthesized on Ni foam through a hydrothermal process. Typically, 180 mg of ammonium fluoride (NH_4F), 300 mg of nickel nitrate hexahydrate ($Ni(NO_3)_2{\cdot}6H_2O$), 130 mg of iron nitrate nonahydrate ($Fe(NO_3)_3{\cdot}9H_2O$), and 300 mg of urea were dissolved in 25 mL of deionized (DI) water at room temperature. The Ni foam (25 mm × 25 mm × 1.5 mm) was thoroughly cleaned with ethanol and water, followed by immersion in the prepared solution. Then, the solution containing the immersed Ni foam was transferred into a Teflon-lined stainless-steel autoclave and kept at 120 °C for 12 h. During the hydrothermal process, NF grew uniformly on the surface of the Ni foam. After cooling to room temperature, the NF was cleaned several times with water and ethanol. Then, they were dried in an oven at 60 °C for later use. In addition, the synthesis method for the MF and CF was similar to the NF, except that the $Ni(NO_3)_2{\cdot}6H_2O$ in the hydrothermal processes was replaced with manganese chloride ($MnCl_2$)and cobalt nitrate hexahydrate ($Co(NO_3)_2{\cdot}6H_2O$).

Synthesis of SOM-Modified Electrocatalysts: SOM-modified electrocatalysts were synthesized through a hydrothermal process. Typically, 40 mg of SOM was dissolved in a mixed solution of 10 mL N,N-dimethylformamide (DMF), and 1 mL DI water. After being fully immersed in the above transparent solution, the NF was transferred into a Teflon-lined stainless-steel autoclave and maintained at 120 °C for 48 h. After cooling to room temperature, the SOM-modified electrocatalysts

were cleaned several times with water and ethanol. Then, they were dried in an oven at 60 °C for later use. Six SOMs were used to modify the electrocatalysts: TA, DA, PA, OA, AA, and NA. As the PA-modified electrocatalysts had the best OER performance in seawater, "SOM-modified electrocatalysts" in the main text generally refers to PA-modified electrocatalysts unless otherwise specified.

Supporting Information

Supporting Information is available from the Wiley Online Library or from the author.

Acknowledgements

The authors gratefully acknowledge the financial support provided by the Australia Research Council (CE230100032, DP230102027, DP240102575, LP210301397, FT200100062). Q.N. acknowledges the financial support from the Chinese CSC Scholarship Program.

Open access publishing facilitated by The University of Adelaide, as part of the Wiley - The University of Adelaide agreement via the Council of Australian University Librarians.

Conflict of Interest

The authors declare no conflict of interest.

Data Availability Statement

The data that support the findings of this study are available from the corresponding author upon reasonable request.

Keywords

ampere-level current density, Cl-mediated electron buffering, oxygen evolution reaction, seawater electrolysis, small organic molecules

Received: February 23, 2025
Revised: March 23, 2025
Published online:

[1] a) S. Dresp, F. Dionigi, S. Loos, J. Ferreira de Araujo, C. Spöri, M. Gliech, H. Dau, P. Strasser, *Adv. Energy Mater.* **2018**, *8*, 1800338; b) S. Dresp, T. Ngo Thanh, M. Klingenhof, S. Brückner, P. Hauke, P. Strasser, *Energy Environ. Sci.* **2020**, *13*, 1725; c) H. Xie, Z. Zhao, T. Liu, Y. Wu, C. Lan, W. Jiang, L. Zhu, Y. Wang, D. Yang, Z. Shao, *Nature* **2022**, *612*, 673; d) R. K. Balaji, F. You, *Energy Environ. Sci.* **2024**, *17*, 6138; e) S. Dresp, F. Dionigi, M. Klingenhof, P. Strasser, *ACS Energy Lett.* **2019**, *4*, 933.

[2] a) H. Becker, J. Murawski, D. V. Shinde, I. E. L. Stephens, G. Hinds, G. Smith, *Sustainable Energy Fuels* **2023**, *7*, 1565; b) J. Tang, C. Su, Z. Shao, *Exploration* **2024**, *4*, 20220112; c) J. Liang, Z. Cai, X. He, Y. Luo, D. Zheng, S. Sun, Q. Liu, L. Li, W. Chu, S. Alfaifi, F. Luo, Y. Yao, B. Tang, X. Sun, *Chem* **2024**, *10*, 3067; d) H. Saada, B. Fabre, G. Loget, G. Benoit, *ACS Energy Lett.* **2024**, *9*, 3351.

[3] a) N. Wang, P. Ou, S.-F. Hung, J. E. Huang, A. Ozden, J. Abed, I. Grigioni, C. Chen, R. K. Miao, Y. Yan, J. Zhang, Z. Wang, R. Dorakhan, A. Badreldin, A. Abdel-Wahab, D. Sinton, Y. Liu, H. Liang, E. H. Sargent, *Adv. Mater.* **2023**, *35*, 2210057; b) L. Zhang, Z. Wang, J. Qiu, *Adv. Mater.* **2022**, *34*, 2109321; c) S. Zhang, Y. Wang, S. Li, Z. Wang, H. Chen, L. Yi, X. Chen, Q. Yang, W. Xu, A. Wang, Z. Lu, *Nat. Commun.* **2023**, *14*, 4822.

[4] a) S. Zhang, W. Xu, H. Chen, Q. Yang, H. Liu, S. Bao, Z. Tian, E. Slavcheva, Z. Lu, *Adv. Mater.* **2024**, *36*, 2311322; b) W. Tong, M. Forster, F. Dionigi, S. Dresp, R. Sadeghi Erami, P. Strasser, A. J. Cowan, P. Farràs, *Nat. Energy* **2020**, *5*, 367.

[5] H. Fei, R. Liu, T. Liu, M. Ju, J. Lei, Z. Wang, S. Wang, Y. Zhang, W. Chen, Z. Wu, M. Ni, J. Wang, *Adv. Mater.* **2024**, *36*, 2309211.

[6] a) Z. Li, G. Lin, L. Wang, H. Lee, J. Du, T. Tang, G. Ding, R. Ren, W. Li, X. Cao, S. Ding, W. Ye, W. Yang, L. Sun, *Nat. Catal.* **2024**, *7*, 944; b) F. Meharban, C. Lin, X. Wu, L. Tan, H. Wang, W. Hu, D. Zhou, X. Li, W. Luo, *Adv. Energy Mater.* **2024**, *14*, 2402886.

[7] a) P. Wang, P. Wang, T. Wu, X. Sun, Y. Zhang, *Adv. Sci.* **2024**, *11*, 2407892; b) W. Liu, J. Yu, M. G. Sendeku, T. Li, W. Gao, G. Yang, Y. Kuang, X. Sun, *Angew. Chem., Int. Ed.* **2023**, *62*, 202309882; c) W. Liu, J. Yu, T. Li, S. Li, B. Ding, X. Guo, A. Cao, Q. Sha, D. Zhou, Y. Kuang, X. Sun, *Nat. Commun.* **2024**, *15*, 4712.

[8] Z. Li, Y. Yao, S. Sun, J. Liang, S. Hong, H. Zhang, C. Yang, X. Zhang, Z. Cai, J. Li, Y. Ren, Y. Luo, D. Zheng, X. He, Q. Liu, Y. Wang, F. Gong, X. Sun, B. Tang, *Angew. Chem., Int. Ed.* **2024**, *63*, 202316522.

[9] W. Xu, Z. Wang, P. Liu, X. Tang, S. Zhang, H. Chen, Q. Yang, X. Chen, Z. Tian, S. Dai, L. Chen, Z. Lu, *Adv. Mater.* **2024**, *36*, 2306062.

[10] X. Kang, F. Yang, Z. Zhang, H. Liu, S. Ge, S. Hu, S. Li, Y. Luo, Q. Yu, Z. Liu, Q. Wang, W. Ren, C. Sun, H.-M. Cheng, B. Liu, *Nat. Commun.* **2023**, *14*, 3607.

[11] Z. Cai, J. Liang, Z. Li, T. Yan, C. Yang, S. Sun, M. Yue, X. Liu, T. Xie, Y. Wang, T. Li, Y. Luo, D. Zheng, Q. Liu, J. Zhao, X. Sun, B. Tang, *Nat. Commun.* **2024**, *15*, 6624.

[12] a) H. Liu, W. Shen, H. Jin, J. Xu, P. Xi, J. Dong, Y. Zheng, S. Qiao, *Angew. Chem., Int. Ed.* **2023**, *62*, 202311674; b) X. Duan, Q. Sha, P. Li, T. Li, G. Yang, W. Liu, E. Yu, D. Zhou, J. Fang, W. Chen, Y. Chen, L. Zheng, J. Liao, Z. Wang, Y. Li, H. Yang, G. Zhang, Z. Zhuang, S.-F. Hung, C. Jing, J. Luo, L. Bai, J. Dong, H. Xiao, W. Liu, Y. Kuang, B. Liu, X. Sun, *Nat. Commun.* **2024**, *15*, 1973.

[13] a) L. Guo, J. Chi, T. Cui, J. Zhu, Y. Xia, H. Guo, J. Lai, L. Wang, *Adv. Energy Mater.* **2024**, *14*, 2400975; b) L. Liao, D. Li, Y. Zhang, Y. Zhang, F. Yu, L. Yang, X. Wang, D. Tang, H. Zhou, *Adv. Mater.* **2024**, *36*, 2405852.

[14] a) P. Zhai, C. Wang, Y. Zhao, Y. Zhang, J. Gao, L. Sun, J. Hou, *Nat. Commun.* **2023**, *14*, 1873; b) Y. Zuo, V. Mastronardi, A. Gamberini, M. I. Zappia, T.-H.-H. Le, M. Prato, S. Dante, S. Bellani, L. Manna, *Adv. Mater.* **2024**, *36*, 2312071.

[15] P. A. Kempler, R. H. Coridan, L. Luo, *Chem. Rev.* **2024**, *124*, 10964.